11.6 Multiscale Modeling of Sickle Cell Anemia

Xuejin Li and Huan Lei

Abstract Sickle cell anemia is a genetic blood disorder exhibiting heterogeneous cell morphology, decreased deformability and abnormal adhesion. The primary pathogenic event of the disease is the intracellular nucleation and polymerization of sickle cell hemoglobin followed by sickling of red blood cells that result in vaso-occlusive crises and other pathophysiological aspects of the disease. In this chapter, we present the morphological, rheological, and adhesive properties of sickle cells, and their relevance to the vaso-occlusion under physiological conditions.

1 Introduction

Sickle cell anemia (SCA) is a genetic disorder of the blood that draws its name from the abnormal sickled shape of the affected red blood cells (RBCs) (Pauling et al 1949; Gravitz and Pincock 2014). It afflicts about 100,000 individuals in the United States and millions of people worldwide (Modell and Darlison 2008). In addition, SCA is one of the most common cause of stroke in children. Despite modern health care and technology, the average lifespan of an individual with SCA in the United States still only hits 40 to 50 years. Patients with SCA have significant morbidity and reduced quality of life as a result of stroke, frequent painful vaso-occlusive crisis events, and other serious clinical complications such as acute chest syndrome (Bunn 1997; Barabino et al 2010).

Xuejin Li
Division of Applied Mathematics, Brown University, Providence, RI 02912, USA; Institute of Fluid Engineering, Zhejiang University, Hangzhou, Zhejiang 310027, P. R. China. e-mail: Xuejin_Li@brown.edu

Huan Lei
Advanced Computing, Mathematics & Data, Pacific Northwest National Laboratory, Richland, WA 99352, USA. e-mail: Huan.Lei@pnnl.gov

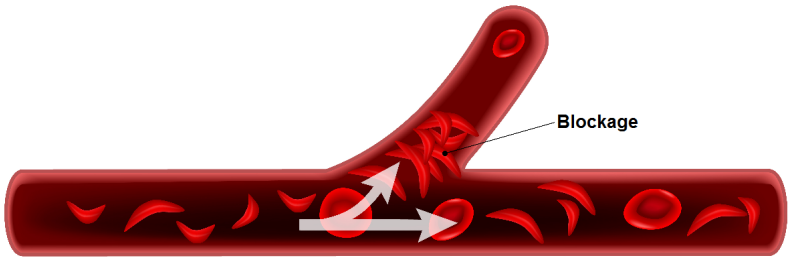

Fig. 1 Vaso-occlusive crisis in SCA. The polymerization of HbS molecules causes cell sickling and damage to the cell membrane. The abnormal, sickle-shaped RBCs obstruct microcapillaries and restrict blood flow leading to vaso-occlusion.

The origin of SCA has been traced to the intracellular polymerization of sickle cell hemoglobin (HbS) under deoxygenation conditions (Hofrichter et al 1974; Noguchi and Schechter 1981), causing a substantial increase in intracellular viscosity and elastic stiffness as well as a severe damage to RBC membrane (Samuel and Briehl 1990; Liu et al 1991). The affected sickle RBCs (SS-RBCs) become stiff, sticky, and abnormally shaped, so they tend to get stuck in the microcirculation and thereby clogging blood flow (Kaul et al 1989; Kaul and Fabry 2004) (Fig. 1). Here, we present experimental and computational studies related to morphological, rheological and adhesive properties of RBCs in SCA.

2 Intracellular polymerization of sickle hemoglobin

SCA is characterized as the first molecular disease (as early as 1947 by Linus Pauling) (Pauling et al 1949), being linked to the mutation of a single nucleotide, from glutamate to valine, in the hemoglobin molecule. The HbS polymerization has been characterized by a double nucleation mechanism (Ferrone et al 1985a,b; Vekilov et al 2008). According to this mechanism, the HbS polymerization process is initiated by homogeneous nucleation in solution and followed by heterogeneous nucleation on pre-existing HbS polymer fibers (Ferrone et al 1985a,b). A different two-step nucleation mechanism has also been proposed (ten Wolde and Frenkel 1997; Shiryayev and Gunton 2004; Lutsko and Nicolis 2006): first, formation of a dense liquid droplet; then, formation of HbS fiber nuclei inside the liquid droplet. Consequently, HbS polymer fibers grow spontaneously and distort the RBCs into abnormal sickle shape.

Numerical models provide valuable insights into the molecular mechanism of HbS fiber nucleation and polymerization. Here, we briefly describe a few of the major achievements. A precursory work was presented by Turner and co-workers (Turner et al 2006), who proposed a theoretical model of HbS polymer fibers and demonstrated that twist plays an essential role in stabilizing the polymerized fibers. Yang et al. performed Metropolis Monte Carlo simulations of self-assembled filamentous

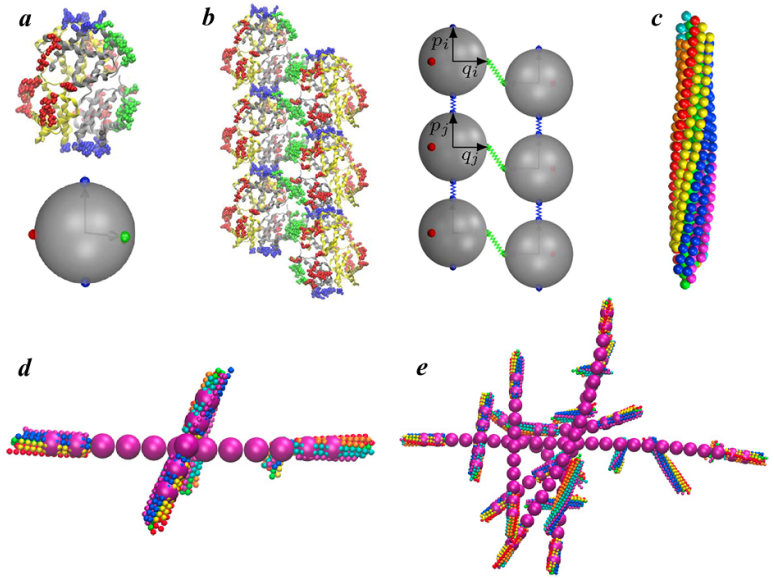

Fig. 2 Mesoscopic modeling of polymerization of HbS. (*a*) Molecular structure of sickle cell hemoglobin (*Upper*) and the corresponding patchy particle model (*Lower*). Green and blue mark the lateral and axial intra-strand contacts, while red marks the inter-strand contacts. (*b*) Double-stranded structure of HbS filament (*Left*) with its representation within patchy particle model. (*c*) HbS filament polymerized from HbS particles. (*d*) Interaction of two growing HbS fibers. (*e*) Modeling fiber bundle and domain formation. Reproduced with permission from (Lu et al 2016, 2017).

bundles (Yang et al 2010). They found that the molecular chirality and attractive interactions can control the assembly size of HbS polymer fibers. Li and Lykotrafitis employed a coarse-grained particle-based HbS model to investigate the mechanical properties of HbS polymer fibers (Li and Lykotrafitis 2011; Li et al 2012). They demonstrate that HbS polymer fiber frustration and compression play a critical role in fiber zipping and unzipping dynamics.

To provide new details of how SCA manifests inside RBCs, we have developed a mesoscopic patchy particle HbS model to study the polymerization of HbS and the fiber growth dynamics (Lu et al 2016). In the patchy particle model, an HbS molecule is modeled by a rigid spherical particle with three patches on its surface, representing the locations of double-stranded contact sites among HbS molecules (Fig. 2*a*). In addition, to model the helical twist effect, we consider an angle-bending potential of two adjacent HbS particles within the same strand (Fig. 2*b*). The corresponding potential is taken as

$$V_a = k_a(\theta - \theta_0)^2, \quad V_l = k_l(\beta - \beta_0)^2, \tag{1}$$

where k_a and k_l are the bending constant, and $\theta = \cos^{-1}(\hat{\mathbf{p}}_i \cdot \hat{\mathbf{p}}_j)$ and $\beta = \cos^{-1}(\hat{\mathbf{q}}_i \cdot \hat{\mathbf{q}}_j)$ are the instantaneous angles between the axial vectors ($\mathbf{p}_i$ and $\mathbf{p}_j$) and lateral

vectors ($\mathbf{q}_i$ and $\mathbf{q}_j$) of these two adjacent HbS particles (Fig. 2*b*), respectively. This HbS model was then employed to simulate the HbS polymerization with pre-existing HbS nuclei (Fig. 2*c*), showing that the growth dynamics of HbS polymer fiber is achieved by the addition of HbS monomers.

The study of intracellular HbS polymerization and consequent RBC sickling provides an important basis for understanding the implications and treatment routes of SCA; however, modeling the integrated process from HbS fiber nucleation and polymerization to RBC sickling and then to vaso-occlusion is challenging due to the multiple temporal and spatial scales of the entire process. To make progress toward understanding the integrated processes, in a follow-up study, we proposed a hybrid HbS fiber model, by coupling the aforementioned microscopic patchy particle model with a mesoscopic HbS polymer fiber model (Lu et al 2017). In this proposed multiscale hybrid model, the function of microscopic patchy particle model is to simulate the dynamic polymerization process of HbS molecules, whereas the mesoscopic fiber model represents the major body of HbS polymer fiber. In addition, the hybrid HbS fiber model undergoes a dynamics coarse-graining process during HbS polymerization through a mesoscopic adaptive resolution scheme (MARS). As a result, the hybrid method reduces the computational cost by reducing the number of degrees of freedom in the HbS polymer fiber model. Herein, it can be used to simulate the HbS polymer fiber growth and branching process. As an attempt, we applied the hybrid HbS fiber model to simulate the growth dynamics of two interacting HbS polymer fibers (Fig. 2*d*) and fiber branching process of multiple HbS polymer fibers (Fig. 2*e*), which shows that the fiber-fiber orientation and interaction range play a key roles in determining the structural and mechanical properties of HbS polymer fibers and filament bundles.

3 Biorheology of sickle RBCs and sickle cell blood

As shown in previous section, SS-RBCs exhibit abnormal shapes due to the interaction between intracellular HbS polymer and the cell membrane. Furthermore, SS-RBC suspensions exhibit abnormal rheology and hemodynamics (Usami et al 1975; Kaul et al 1983; Kaul and Xue 1991; Kaul and Liu 1999) due to the heterogeneous cell morphology and elevated cell rigidity (Evans et al 1984; Itoh et al 1995). In this section, we employ the constructed SS-RBC model to investigate the abnormal rheology and hemodynamics of SS-RBC suspension under shear and tube flow.

Since the collective properties of the SS-RBC suspension is mainly determined by the cell morphology and rigidity, we ignore the modeling of intracellular HbS polymer on molecular level. Alternatively, we directly model the interaction between the intracellular polymer and the cell membrance as the stretching force applied on the cell membrane exerted by the growing HbS fibers. As shown in Fig. 3, the letters “A”, “B”, “C” and “D” represent four anchor points where the intracellular growing fibers can potentially approach the cell membrane. Depending on the MCHC, the intracellular HbS polymer may exhibits different configuration. Ac-

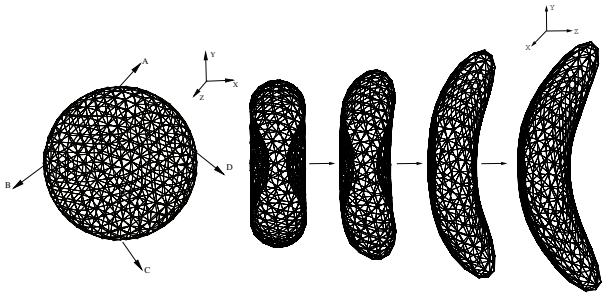

Fig. 3 Left: triangulated mesh of the RBC membrane. The label "A", "B", "C" and "D" represents the four anchor points where the stretching force is applied. Right: Successive snapshots of a RBC during the morphological transition to the "sickle" shape. (From (Lei and Karnidakis 2012)).

cordingly, as the growing HbS fibers may approach the cell membrane from multiple directions, various stretching forces are applied on the four anchor points. Detail simulation parameters are summarized in Tab. 1.

	A	B	C	D
S	$(0,55,54)$	$(0,0,0)$	$(0,-55,54)$	$(0,0,0)$
G	$(0,23,31)$	$(-23,0,31)$	$(0-23,31)$	$(23,0,31)$
E	$(0,55,11)$	$(0,0,0)$	$(0,-55,-11)$	$(0,0,0)$

Table 1 Stretching force (pN) applied on the anchor points for each type of the cell morphology along x, y and z direction. "A", "B", "C", "D" represents the anchor points sketched in Fig. 3.

With the constructed SS-RBCs of various morphologies, we investigate the abnormal rheology of SS-RBC suspension in shear flow. We first consider the shear flow system with hematocrit Hct = 45% following the previous experiment (Usami et al 1975). The viscosity of blood plasma is chosen to be $\eta_0 = 1.2$ cp. Fig. 4 shows the viscosity computed for both healthy and diseased blood under different shear rates. For both types of blood, good agreement with the experimental results is obtained. It is well-known that healthy blood behaves as non-Newtonian fluid with shear-dependent viscosity (Fedosov et al 2011). Under high shear rate, blood cells undergo large deformation with fluid properties pronounced; in contrast, blood cells behave as solid-like, less deformed under low shear rate conditions, resulting in relatively higher viscosity. Therefore, the viscosity of healthy blood increases as the shear rate decreases, as shown in Fig. 4. On the other hand, the deoxygenated SS-RBC suspension shows elevated viscosity values, which are nearly independent of the shear rate. This result is mainly due to the largely elevated cell rigidity; the deoxygenated SS-RBC cannot be deformed under the high shear rate employed in the experiment (Usami et al 1975). Therefore, SS-RBCs exhibit "solid" behavior throughout the entire shear rate regime, leading to this transition from non-Newtonian to Newtonian flow.

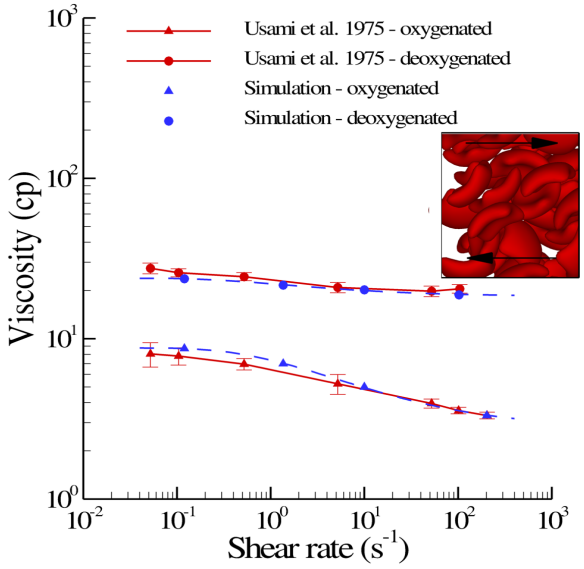

Fig. 4 Shear viscosity of the healthy blood and SS-RBC suspensions with Hct = 45%. The dash lines represent the fitted curve to the simulation result by $\eta = be^{-a/\dot{\gamma}^{0.5}} + c$, where $\dot{\gamma}$ is the shear rate. a, b and c equal to $1.43s^{-1/2}, -6.04\text{cp}, 8.78\text{cp}$ for healthy blood and $1.08s^{-1/2}, -5.5\text{cp}, 23.9\text{cp}$ for deoxygenated SS-RBC suspension. The inset plot shows a snapshot of the "granular" SS-RBCs in shear flow. (From (Lei and Karnidakis 2012)).

Furthermore, experimental studies show that the rheology of SS-RBC suspension further depends on the morphology of the SS-RBCs. Kaul et al. investigated the shear viscosity of SS-RBC suspensions subjected to both fast and gradual deoxygenation procedures (Kaul and Xue 1991) was measured. Two distinct stages were observed for SS-RBC suspensions subjected to the fast deoxygenation. The shear viscosity of the SS-RBC suspensions exhibits fast elevation within the first 7 mins of deoxygenation accompanied with the cell morphology transition to granular shape. However, the shear viscosity gradually decreased during increased deoxygenation, accompanied with a large portion of cells transitioned into extremely elongated shape with the intracellular HbS fibers aligned in one direction. In contrast, SS-RBC suspensions subjected to gradual deoxygenation procedure showed monotonic elevation of shear viscosity and the formation of the sickle shape of blood cells over a period of 30 mins until the full deoxygenated state was achieved. Following this experimental study, we computed the shear viscosity of SS-RBC suspensions with the three distinct types of sickle cell reported in the experiment (Hct = 40%). Fig. 5 shows the shear viscosity values under shear rate from 25 to 75 s^{-1} with similar cell rigidity applied to all the three types. Similar to Fig. 4, the SS-RBC suspensions show shear-independent Newtonian behavior. Moreover, shear viscos-

ity further depends on individual cell shapes, with the value 13.8, 13.1 and 9.6 cp for the granular, sickle and elongated shape, respectively. The simulation results are consistent with the experimentally observed progressive decrease of the viscosity during the increased deoxygenation, since a large portion of granular cell transforms into the elongated shape during the procedure. This result reveals the heterogeneous "effective volume" among the different types of SS-RBC under the shear flow system (Kaul and Xue 1991). Given the same Hct, heterogeneous cell morphologies may further affect the momentum transport between the cells, resulting in different shear viscosity values.

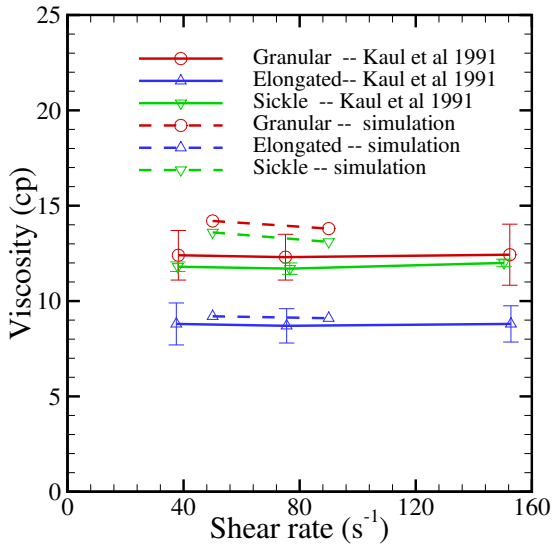

Fig. 5 Shear viscosity of the sickle blood flow with different cell morphologies reported in Ref. (Kaul and Xue 1991), Hct = 40%. (From (Lei and Karnidakis 2012)).

Next, we further examine the hemodynamics of SS-RBC suspensions in an isolated vasculature with different cell groups. While the oxygenated SS-RBC suspensions exhibit hemodynamics similar to healthy blood flow, the deoxygenated SS-RBC suspensions show heterogeneous hemodynamics among the different cell groups. Similar to the experimental study (Kaul et al 1983), we simulate SS-RBC suspensions in a tube flow system with Hct = 30%. We set the diameter of the tube to $9.0\mu m$ as in capillary flow, since the detailed size and topology information of the microvasculature for the experiment is unknown. In this sense, we do not expect the apparent viscosity obtained from the simulation to match exactly with the experiment results. Instead, we focus on the effect of different SS-RBCs groups on the flow resistance in the microcirculation.

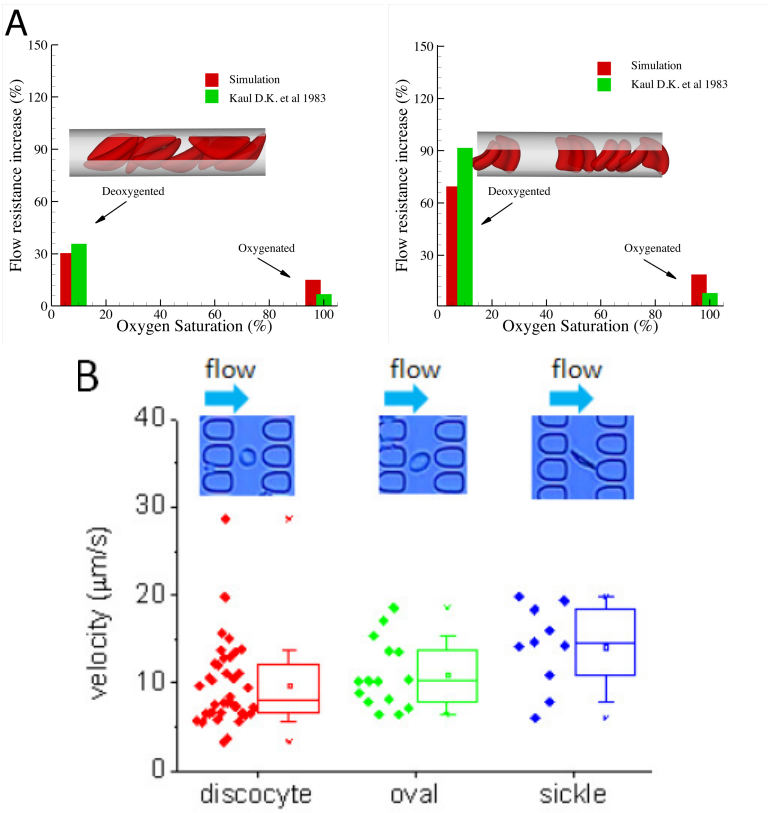

Fig. 6 Top: Increase of the flow resistance induced by the sickle blood flow for both granular and sickle shapes. The inset plot shows a snapshot of the sickle cells in the tube flow. Bottom: Experimental study on SS-RBC cell transition velocity for different cell morphologies through a periodic array of obstacles in microchannel, provided by Du and Dao at MIT. (From (Lei and Karnidakis 2012)).

Deoxygenated blood flow is modeled as a suspension of SS-RBCs with sickle and granular shapes, where the same cell rigidity is applied to both cell groups. The viscosity of the cytosol is set to $4\eta_0$ and $50\eta_0$ for the healthy and deoxygenated blood flow, where $\eta_0 = 1.2$ cp is the viscosity of the blood plasma. The increase of the flow resistance for the sickle and granular shapes under different oxygen tensions is shown in Fig. 6(a). While SS-RBC suspension of both cell groups show further increased flow resistance at deoxygenated state, the granular type of blood flow shows a more pronounced elevation compared with the sickle shape. This result is also consistent with the experimental study of SS-RBCs transiting in a micro-fluidic channel conducted by E. Du and M. Dao (Du et al 2015). Fig. 6(b) shows the transit velocities of individual SS-RBCs with different cell morphologies (discocyte, oval,

sickle) through a periodic array of obstacles (4μm between the two obstacles). The cell group of the "sickle" shape exhibits the largest cell velocity.

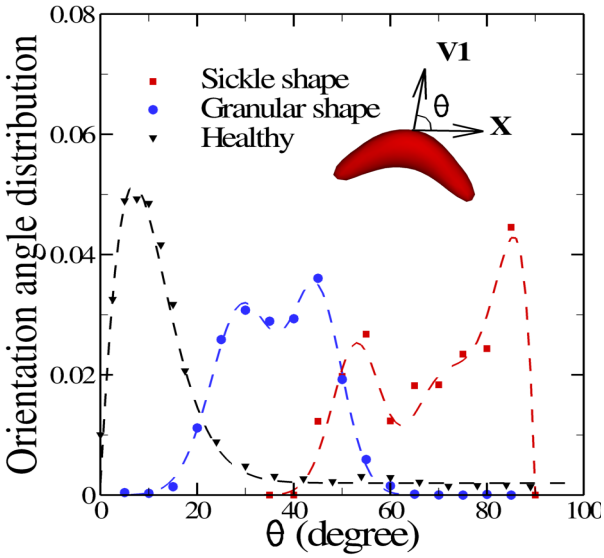

Fig. 7 Cell orientation angle distribution $f(\theta)$ for healthy, sickle and granular cells in pipe flow. The cell orientation is defined by the angle θ between the flow direction (x) and the eigenvector $V1$ of the gyration tensor, as shown in the inset plot. (From (Lei and Karnidakis 2012)).

One possible explanation for the above result, as proposed by the Kaul et al., is the different orientational distribution of SS-RBCs in the capillary: a cell of sickle shape tends to flow along the axis of the tube as also observed by La Celle et al. in experimental studies in (LaCelle 1977). This is consistent with the inset snapshots of the sickle and granular cells in Fig. 6(a). To quantify this phenomenon, we computed the *cell orientation angle distribution* for different cell groups in the tube flow, as shown in Fig. 7. The cell orientation is defined by the angle θ between the flow direction and the eigenvector of the gyration tensor V_1 defined by

$$G_{mn} = \frac{1}{N_v}\sum_i (r_m^i - r_m^C)(r_n^i - r_n^C), \tag{2}$$

where r^i is the coordinate of RBC vertex i, r^C is the center-of-mass coordinate, and m, n represent the x, y, or z direction. λ_1, λ_2 and λ_3 represent the three eigenvalues obtained from the gyration tensor, where $\lambda_1 < \lambda_2 < \lambda_3$. Compared with the granular cell, the orientation angle of the sickle cell shows a wider distribution for larger value, indicating that the sickle shape SS-RBCs are more likely to orient along the

flow direction, which results in a lower flow resistance compared with the granular cells.

Finally, we note that the simulation of SS-RBC suspension in tube flow does not induce blood occlusion in the present study. We performed several sets of simulations with different combinations of cell rigidities and cytosol viscosity; however, no full occlusion was observed in any of these simulations. Moreover, the sickle shape SS-RBC, the widely believed pre-cursor of the vaso-occlusion crisis, actually may result in lower flow resistance than other cell groups. We note that this is mainly due to the omission of the cell-endothelium adhesive interaction in the present study; we address this issue in the next section.

4 Adhesive properties of sickle RBCs

Vaso-occlusion crisis may trigger serious stroke or death for SCA patients. Early experimental studies suggested that this crisis is triggered by the blockage of single sickle/elongated SS-RBC in capillaries, later studies (Kaul et al 1989, 1994; Kaul and Fabry 2004; Barabino et al 2010) have shown that vaso-occlusion mainly occurs in post-capillaries (the microvasculatures following the capillaries). Moreover, some studies demonstrated that there exists no direct correlation between the percentage of the dense SS-RBCs and the disease severity (Ballas et al 1988). Recent studies further revealed that vaso-occlusion is a complex process triggered by the interactions between multiple cell groups (Ballas and Mohandas 2004; Chiang and Frenette 2005; Turhan et al 2002). In this section, we employ computational approach to explore the mechanism of the vaso-occlusion in SCA.

4.1 Adhesive dynamics

In vitro studies by Barabino *et al.* (Barabino et al 1987) show that SS-RBCs exhibit heterogeneous cell adhesivity among different density groups. The light density group shows the largest adhesion while the densest irreversible sickle cells (ISCs) shows the least adhesion. *Ex vivo* studies by Kaul *et al.* (Kaul et al 1994) further examined the alteration of SS-RBC adhesivity after a dehydration/rehydration treatment on individual cell groups and found that the cell adhesivity of the deformable SS2 and the dense SS4 cells can be reversed after controlled treatment. They suspected that different cell groups have similar "adhesion potential", while the heterogeneous cell adhesivity is mainly attributed to the different cell morphological and bio-mechanical properties among the multiple cell density group. Accordingly, we investigate this hypothesis by simulating the adhesive dynamic of SS-RBCs with different cell rigidity and morphologies.

As shown in Fig. 8, we consider three different SS-RBCs under shear flow. Cell I represents a SS2 deformable discocyte. The cell rigidity is similar to the

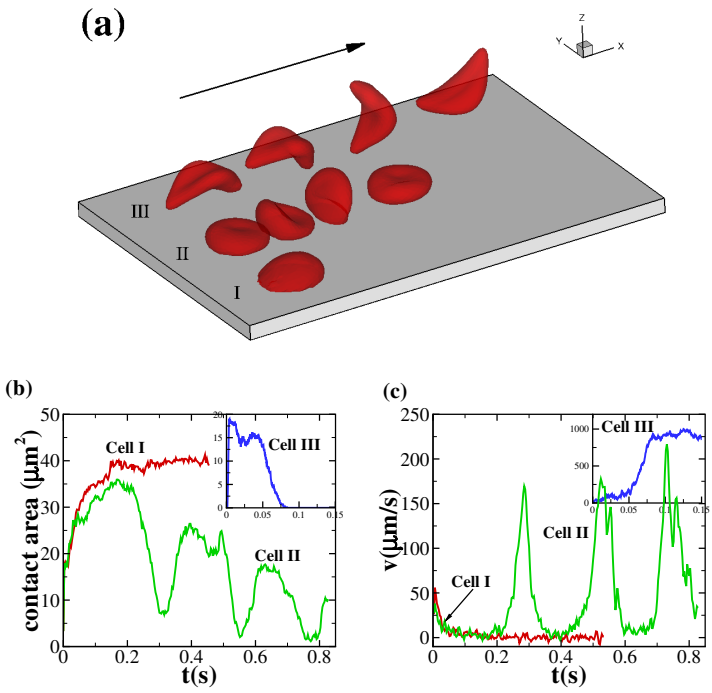

Fig. 8 Sickle cells in shear flow: (a) Successive snapshots of SS-RBCs in shear flow. The labels I, II and III correspond to a deformable SS2 cell, rigid SS3 cell and ISC, respectively. The arrow indicates the flow direction. (b - c) Instantaneous contact area and velocity for SS-RBC in shear flow conditions. (From (Lei and Karniadakis 2013)).

healthy RBC and we set the shear modulus $\mu_0 = 6.8\mu N/m$ and bending rigidity $k_{c0} = 2.4 \times 10^{-19} J$, i.e., similar to healthy cell rigidity (Hupert and Baumann 2003; Mills et al 2004; Suresh et al 2005). Cell III represents an ISC generated through the deoxygenation-reoxygenation process; we set the shear modulus $\mu = 10\mu_0$ following (Itoh et al 1995; Clark et al 1980). Modification to cell bending rigidity in the deoxygenation-reoxygenation process is unknown; here we set $k_c = 10k_{c0}$ and also conduct sensitivity studies. Cell II represents a rigid discocyte (Evans and Mohandas 1987) with medium MCHC value; we set $\mu = 3\mu_0$ and $k_c = 3k_{c0}$ for the comparative study.

Following Kaul et al (1994), we assume that the three cells have similar "adhesive potential," and set identical adhesive parameters. With the same shear rate $\dot{\gamma} = 192s^{-1}$, the three cells exhibit substantially different adhesive dynamics as shown in Fig. 8(a). Cell I exhibits firm adhesion to the lower plate with contact area around $40.5\mu m^2$. Cell II, however, shows weaker adhesivity than Cell I. Although it also exhibits transient adhesion to the lower plate initially, it undergoes a periodic flip movement along the flow direction and eventually detaches from the plate after two to three flips, as characterized by the peak values of the instantaneous

cell velocity at 0.30, 0.53 and 0.72s. Accordingly, the contact area achieves minimum values at those times. Different from cells I and II, cell III does not show any adhesion to the plate; instead, it directly detaches from the lower plate and moves freely without adhesive bonds established thereafter. Given the same "adhesive potential", the present results validate the hypothesis that heterogeneous cell adhesive dynamics is mainly due to the different cell rigidities and peculiar cell morphologies. To further investigate this effect, we use free energy analysis to quantify the cell adhesion in static condition.

We compute the instantaneous contact area for each cell until steady state is reached, as shown in Fig. 9(a). While the contact area for all of the cells increases sharply to 10 μm^2 within the initial stage, the contact area between the plate and cell I and II further increases to 30 μm^2 and 21 μm^2 at the later stage. This inverse relationship is consistent with the different cell adhesive dynamics in shear flow system, and it can be understood by the free energy analysis during the adhesion process. If we define the cell and the ligand particles as a single system, the change of total free energy ΔE during the process can be written as

$$\Delta E = \Delta E_{deform} - \Delta E_{adhesion}, \tag{3}$$

where ΔE_{deform} represents the increase of the cell free energy due to the deviation of cell shape from the equilibrium state. $\Delta E_{adhesion}$ represents the absolute value of the energy decrease due to the adhesive bond formation between the cell and the ligand particles. The final state is determined by the balance between the two free energy terms. A deformable SS2 cell is prone to form larger contact area than the rigid cell; it can be understood as follows. For SS2 cell with smaller cell rigidity, the energy barrier induced by the cell deformation is relatively small, and free energy decrease induced by cell adhesion plays a dominant role, resulting in further cell deformation and larger cell contact area. In contrast, the rigid SS4 cell exhibits "solid" like properties with a larger energy barrier for cell deformation. The adhesive interaction between the cell and plate is more like the attraction between two solid objects where the cell deformation plays a less important role. After the initial incubation stage, the adhesive interaction driven by the bond formation cannot overcome the free energy increase induced by the cell deformation, and therefore it prohibits further increase of the contact area.

Fig. 9(b) shows the ΔE_{deform} as a function of the contact area ΔA for the three cells induced by different adhesive affinities. The numerical results are fitted by $\alpha \Delta A^4$, where α depends on the cell rigidity of individual cells. The adhesion free energy $\Delta E_{adhesion}$ can be approximated by $\beta \Delta A$, where β is the energy coefficient determined by the adhesive affinity. In the present work, the adhesive interaction is modeled by the adhesive bond interaction between ligands coated on the substrate and the receptors on the cell membrane. While each receptor on cell membrane can form multiple adhesive bonds with ligands, each ligand can only form one adhesive bond with the receptor. Therefore, β can be approximated by $k_s l_s^2 n_{ligand}$, where k_s is the adhesive spring bond constant, l_s is the cut-off length of the adhesive bond interaction, and n_{ligand} is number density of the ligands on the substrate. The equilibrium

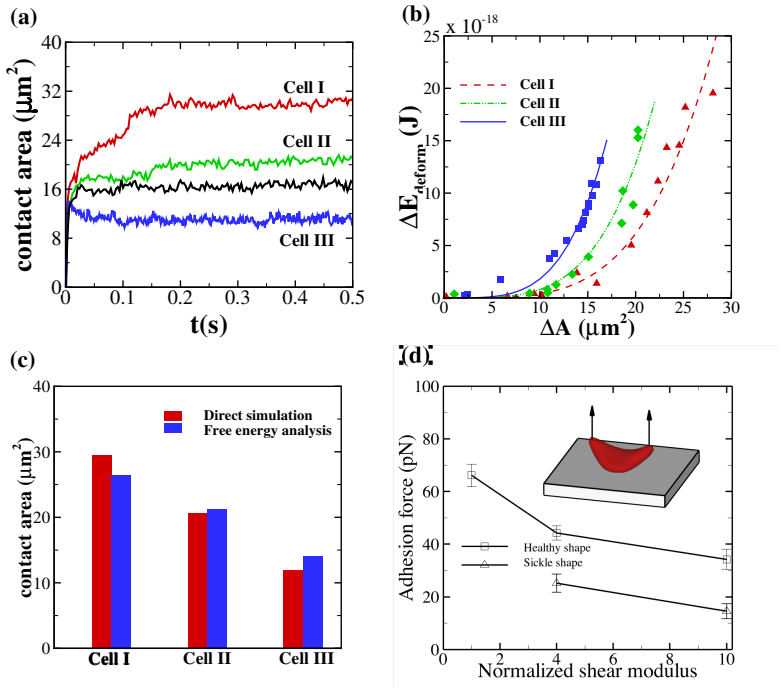

Fig. 9 Adhesion in static conditions: (a) Instantaneous contact area between the SS-RBC and the plate coated with adhesive ligands. The black curve represents the contact area of a discocyte with cell rigidity similar to the ISC (cell III). (b) Increase of the cell free energy as a function of the contact area. (c) Cell contact area ΔA computed from direct simulation and free energy analysis by Eq. (4). (d) Adhesive force between the cell and the plate as a function of the membrane rigidities for cell morphologies. The error bar represents the adhesive force computed from four independent simulations. The inset plot shows a sketch of the simulation set up, where a uniform lift force is applied on the upper part of an ISC. (From (Lei and Karniadakis 2013)).

state is determined as the state with minimum free energy term, *e.g.*

$$\Delta A = \left(\frac{\beta}{4\alpha}\right)^{1/3}. \tag{4}$$

According to Fig. 9(b), α is about $3.8 \times 10^{25}\ J/m^8$, $8.0 \times 10^{25}\ J/m^8$ and $1.8 \times 10^{26}\ J/m^8$ for cell I, II and III. The yields the contact area $A = A_0 + \Delta A$ approximately 26.5 μm^2, 21.3 $\mu m^2$and 14.0 μm^2 for cell I, II and III, where A_0 is the initial contact area without any adhesion, which is 3.5 μm^2 for cell I and II, and 0.6 μm^2 for cell III. This result agrees well with the direct simulation results of 29.5 μm^2, 20.7 μm^2 and 12.0 μm^2, as shown in Fig. 9(c). Compared with the shear flow system, the contact area of cell I computed in static condition is smaller. This discrepancy is mainly due to the increased cell deformation induced by the hydrodynamic interaction under shear flow condition. The extended cell membrane facilitates the bond formation

and result in larger contact area. For cell III, we note that the contact area is smaller than the value for a discocyte with similar cell rigidity. This result indicates that the peculiar cell morphology may further affect the cell adhesivity.

To quantify the effects discussed above, we directly compute the adhesive force between the plate and SS-RBCs with different cell rigidities and morphologies. The adhesive force is determined as the lift force that detach the cell from the plate in quasi-static process, as shown in Fig. 9(d). Similar to the contact area, the adhesive force also exhibits an inverse relationship with the cell rigidity. Moreover, compared with the discocyte, the ISC exhibits smaller adhesive force given the similar cell rigidity, indicating less adhesivity induced by its peculiar cell morphology.

4.2 Vaso-occlusion crisis

We model blood circulation of SS-RBC suspensions in post-capillaries as in a tube with diameter $D = 10\mu m$ and hematocrit Hct = 30% similar to (Kaul et al 1989, 1994). As shown in Fig. 10, small green particles represent the adhesive ligands which can interact with the SS-RBCs. To quantify the distinct role of different cell groups, we infuse suspensions of different cell groups into the tube by applying a pressure gradient $\Delta P/\Delta x = 8.7 \times 10^4 Pa/m$.

First, we consider suspensions composed of SS2 cells (labeled by blue) and ISC cells (labeled by red) with ratio 1 : 1. We prepare the steady flow by turning off the adhesive interaction. The mean flow velocity at the initial stage is round 150 $\mu m/s$. Starting from the steady state (t = 0 s), we turn on the adhesive interaction between the SS-RBCs and the ligand particles and compute the instantaneous flow velocity across the tube, as represented by the red curve in Fig. 10. Blood flow maintains steady state until one of the SS2 cells adheres to the vessel wall, triggering a sharp decrease of blood flow around $t = 0.5$ s. As a positive feedback, the decreased blood flow induces more SS2 cells adherent to the vessel wall, leading to a further decrease of flow rate at t = 0.63 s and t = 0.7 s. Moreover, these adherent cells decrease the effective vessel lumen near the adherent region resulting in a secondary trapping of the ISC groups. The final occlusion state is reached around $t \approx 2$ s with cell patterns similar to the experimental observations (Kaul et al 1989, 1994). This result demonstrates that under physiological conditions similar to microcirculation in post-capillaries, the *interplay* of deformable SS2 cells and ISCs can potentially trigger full blood occlusion. Although the same adhesive parameters are applied to the two cell groups, no adherent ISC is observed in the present simulations. Several independent sets of simulation were conducted with different initial conditions and similar patterns of full occlusion were observed.

To identify the unique contribution of the deformable SS2 cell group, we performed a similar simulation for suspension consisting of ISC and healthy RBCs. Starting from the steady flow at t = 0 s, we compute the instantaneous velocity of the blood suspension for 6 s, as represented by the green line in Fig. 10. Blood flow shows decreased velocity due to the ISC-ligand interaction, where transient adhesive

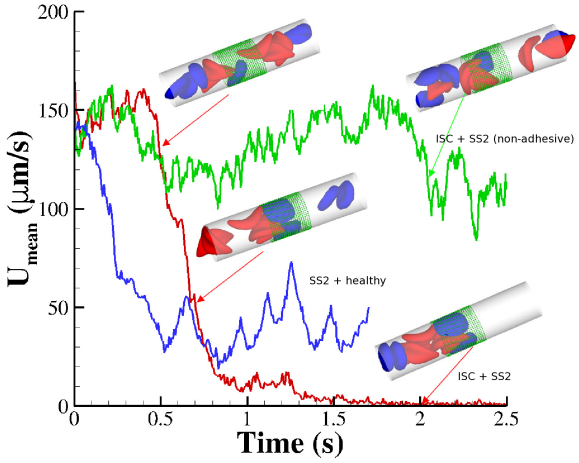

Fig. 10 Vaso-occlusion in post-capillaries: instantaneous mean velocity of blood flow in a cylindrical tube of $D = 10\mu m$ infused with different SS-RBC suspensions. The red curve represents the resultant velocity infused with SS2 and ISC cell groups. The inset plots represent the instantaneous snapshots where SS2 cells adhere to vessel wall, consequently trapping the ISCs and resulting in cell blockage. The green curve represents the blood velocity infused with SS2 and ISC cell groups, where adhesive interaction is only applied to the ISC group. The time axis is scaled by 0.5 for better visualization. The inset plot represents a snapshot where transient adhesion is established between ISC and the tube wall. Steady flow is recovered as the cell detaches from the tube wall. The blue curve represents the instantaneous velocity of blood flow infused with SS2 and healthy cell groups. Blood flow exhibits a slow down but not a full occlusion. (From (Lei and Karniadakis 2013)).

bonds can be formed. However, blood occlusion is not observed in this simulation since blood flow can recover the initial flow rate when the adherent ISCs detach from the tube wall, as consistently observed in *ex vivo* studies (Kaul et al 1994), where the ISCs, when infused alone, did not result in microvascular blockage. This result reveals the specific contribution of the SS2 cell group in the vaso-occlusion crisis and is consistent with clinical investigation results (Ballas et al 1988).

In contrast, the ISC cell group, contributes differently to the occlusion crisis. We investigate its unique contribution by simulating the blood suspension mixed with the deformable SS2 and healthy cells. Starting from the steady flow at $t = 0\ s$, we compute the instantaneous velocity of the blood flow, as represented by the blue line in Fig. 10. Although blood flow slows down due to the cell adhesion at $t = 0.25\ s$ and $t = 0.48\ s$, full occlusion is not observed in the present simulation. In particular, we find that healthy RBCs can squeeze through the sieve-like region formed by adherent SS2 cells due to its high deformability. The present result, in turn, identifies the specific contribution of the ISC group in the vaso-occlusion crisis. Although the ISC group may not participate in the cell adhesive interaction with the vascular wall, it serves as the particular cell group trapped by adherent cells in the post-capillaries.

Besides the cell interaction among the SS-RBCs, recent studies (Kaul and Hebbel 2000) have shown that SCA is often accompanied with an inflammatory endothelial phenotype with elevated leukocyte recruitment in blood circulation, where the inflammation-stimulated leukocytes may further interact with SS-RBC, leading to blood occlusion in venular flow. We refer to Refs. (Turhan et al 2002; Lei and Karniadakis 2013) for details.

5 Summary

In this chapter, we overview the pathogenesis of vaso-occlusive crisis in sickle cell anemia (SCA) that involves several processes across multiple time and length scales. We cover the morphological, rheological and adhesive abnormalities of sickle red blood cells, and discuss individual and environmental factors underlying the process of SCA vaso-occlusion. The genetic basis and molecular causes of the disease has been understood for more than half a century; however, progress in developing treatments to prevent painful vaso-occlusion and the other myriad of associated symptoms has been slow. Therefore, the need to develop new therapeutic interventions and treatment strategies for SCA remains paramount.

Acknowledgements This work was supported, in part, by the National Institutes of Health (NIH) under grants U01HL114476 and U01HL116323.

References

Ballas SK, Mohandas N (2004) Sickle red cell microrheology and sickle blood rheology. Microcirculation 11:209–225

Ballas SK, Larner J, Smith ED, Surrey S, Schwartz E, Rappaport EF (1988) Rheologic predictors of the severity of the painful sickle cell crisis. Blood 72:1216–1223

Barabino GA, McIntire LV, Eskin SG, Sears DA, Udden M (1987) Endothelial cell interactions with sickle cells, sickle cell, sickle trait, mechanically injured, and normal erythrocytes under controlled flow. Blood 70:152–157

Barabino GA, Platt MO, Kaul DK (2010) Sickle cell biomechanics. Annu Rev Biomed Eng 12:345–367

Bunn HF (1997) Pathogenesis and treatment of sickle cell disease. N Engl J Med 337:762–769

Chiang EY, Frenette PS (2005) Sickle cell vaso-occlusion. Hematol Oncol Clin North Am 19:771–784

Clark MR, Mohandas N, Shohet SB (1980) Deformability of oxygenated irrversibly sickled cells. J Clin Invest 65:189–196

Du E, Diez-Silva M, Kato GJ, Dao M, Suresh S (2015) Kinetics of sickle cell biorheology and implications for painful vasoocclusive crisis. Proc Natl Acad Sci USA 112:1422–1427

Evans E, Mohandas N (1987) Membrane-associated sickle hemoglobin: a major determinant of sickle erythrocyte rigidity. Blood 70:1443–1449

Evans E, Mohandas N, Leung A (1984) Static and dynamic rigidities of normal and sickle erythrocytes. major influence of cell hemoglobin concentration. J Clin Invest 73:477–488

Fedosov DA, Pan W, Caswell B, Gompper G, Karniadakis GE (2011) Predicting human blood viscosity in silico. Proc Natl Acad Sci USA 108(29):11,772–11,777

Ferrone FA, Hofrichter J, Eaton WA (1985a) Kinetics of sickle hemoglobin polymerization. I. studies using temperature-jump and laser photolysis techniques. J Mol Biol 183:591–610

Ferrone FA, Hofrichter J, Eaton WA (1985b) Kinetics of sickle hemoglobin polymerization. II. a double nucleation mechanism. J Mol Biol 183:611–631

Gravitz L, Pincock S (2014) Sickle-cell disease. Nature 515:S1

Hofrichter H, Ross PD, Eaton WA (1974) Kinetics and mechanism of deoxyhemoglobin s gelation: a new approach to understanding sickle cell disease. Proc Natl Acad Sci USA 71:4864–4868

Hupert C, Baumann M (2003) Local membrane curvature affects spontaneous membrane fluctuation characteristics. Mol Membr Biol 20:155–162

Itoh T, Chien S, Usami S (1995) Effects of hemoglobin concentration on deformability of individual sickle cells after deoxygenation. Blood 85:2245–2253

Kaul DK, Fabry ME (2004) In *vivo* studies of sickle red blood cells. Microcirculation 11:153–165

Kaul DK, Hebbel RP (2000) Hypoxia/reoxygenation causes inflammatory response in transgenic sickle mice but not in normal mice. J Clin Invest 106:411–420

Kaul DK, Liu X (1999) Rate of deoxygenation modulates rheologic behavior of sickle red blood cells at a given mean corpuscular hemoglobin concentration. Clin Hemorheol Microcirc 21:125–135

Kaul DK, Xue H (1991) Rate of deoxygenation and rheologic behavior of blood in sickle cell anemia. Blood 77:1353–1361

Kaul DK, Fabry ME, Windisch P, Baez S, Nagel RL (1983) Erythrocytes in sickle-cell-anemia are heterogeneous in their rheological and hemodynamic characteristics. J Clin Invest 72:22–31

Kaul DK, Fabry ME, Nagel RL (1989) Microvascular sites and characteristics of sickle cell adhesion to vascular endothelium in shear flow conditions: Pathophysiological implications. Proc Natl Acad Sci USA 86:3356–3360

Kaul DK, Chen D, Zhan J (1994) Adhesion of sickle cells to vascular endothelium is critically dependent on changes in density and shape of the cells. Blood 83:3006–3017

LaCelle PL (1977) Oxygen delivery to muscle cells during capillary vascular occlusion by sickle erythrocytes. Blood Cells 3:263–272

Lei H, Karniadakis GE (2013) Probing vasoocclusion phenomena in sickle cell anemia via mesoscopic simulations. Proc Natl Acad Sci USA 110:11,326–11,330

Lei H, Karnidakis GE (2012) Quantifying the rheological and hemodynamic characteristics of sickle cell anemia. Biophys Journal 102:185–194

Li H, Lykotrafitis G (2011) A coarse-grain molecular dynamics model for sickle hemoglobin fibers. J Mech Behav Biomed Mater 4:162–173

Li H, Ha V, Lykotrafitis G (2012) Modeling sickle hemoglobin fibers as one chain of coarse-grained particles. J Biomech 45:1947–1951

Liu SC, Derick LH, Zhai S, Palek J (1991) Uncoupling of the spectrin-based skeleton from the lipid bilayer in sickled red cells. Science 252:574–576

Lu L, Li H, Bian X, Li X, Karniadakis GE (2017) Mesoscopic adaptive resolution scheme toward understanding of interactions between sickle cell fibers. Biophys J 113:48–59

Lu X, Wood DK, Higgins JM (2016) Deoxygenation reduces sickle cell blood flow at arterial oxygen tension. Biophys J 110:2751–2758

Lutsko JF, Nicolis G (2006) Theoretical evidence for a dense fluid precursor to crystallization. Phys Rev Lett 96:46,102

Mills JP, Qie L, Lim CT, Dao M, Suresh S (2004) Nonlinear elastic and viscoelastic deformation of the human red blood cell with optical tweezers. Mech Chem Biosyst 1(3):169–180

Modell B, Darlison M (2008) Epidemiology of haemoglobin disorders and derived service indicators. Bull World Health Organ 86:480–487

Noguchi CT, Schechter AN (1981) The intracellular polymerization of sickle hemoglobin and its relevance to sickle cell disease. Blood 58:1057–1069

Pauling L, Itano HA, Singer SJ, Wells IC (1949) Sickle cell anemia, a molecular disease. Science 110:543–548

Samuel RE, Briehl RW (1990) Nucleation and growth of fibres and gel formation in sickle cell hemoglobin. Nature 345:833–835

Shiryayev A, Gunton JD (2004) Crystal nucleation for a model of globular proteins. J Chem Phys 120:8318–8326

Suresh S, Spatz J, Mills JP, Micoulet A, Dao M, Lim CT, Beil M, Seufferlein T (2005) Connections between single-cell biomechanics and human disease states: gastrointestinal cancer and malaria. Acta Biomaterialia 1:15–30

ten Wolde PR, Frenkel D (1997) Enhancement of protein crystal nucleation by critical density fluctuations. Science 277:1975–1978

Turhan A, Weiss LA, Mohanda N, Coller BS, Frenette PS (2002) Primary role for adherent leukocytes in sickle cell vascular occlusion: A new paradigm. Proc Natl Acad Sci USA 99:3047–3051

Turner M, Briehl R, Wang J, Ferrone F, Josephs R (2006) Anisotropy in sickle hemoglobin fibers from variations in bending and twist. J Mol Biol 357:1422–1427

Usami S, Chien S, Scholtz PM, Bertles JF (1975) Effects of deoxygenation on blood rheology in sickle cell disease. Microvasc Res 9:324–334

Vekilov P, Galkin O, Pettitt B, Choudhury N, Nagel R (2008) Determination of the transition-state entropy for aggregation suggests how the growth of sickle cell hemoglobin polymers can be slowed. J Mol Biol 377:882–888

Yang YS, Meyer RB, Hagan MF (2010) Self-limited self-assembly of chiral filaments. Phys Rev Lett 104:258,102